Nonlinear helicity anomalies in the cyclotron resonance photoresistance of two-dimensional electron systems

E. Mönch [1] , S. Schweiss [1] , I. Yahniuk,[1] M. L. Savchenko,[2] I. A. Dmitriev [1] , A. Shuvaev [2]
A. Pimenov,[2] D. Schuh,[1] D. Bougeard,[1] and S. D. Ganichev [1,3,*]

[1]*Terahertz Center, University of Regensburg, 93040 Regensburg, Germany*
[2]*Institute of Solid State Physics, Vienna University of Technology, 1040 Vienna, Austria*
[3]*CENTERA LAB, Centre for Advanced Materials and Technology CEZAMAT, Warsaw University of Technology, 02 - 822 Warsaw, Poland*

Our studies of the cyclotron resonance (CR) photoresistance in GaAs-based two-dimensional electron systems (2DES) reveal an anomalously low sensitivity to the helicity of the incoming circularly polarized terahertz radiation. We find that this anomaly is strongly intensity dependent, and the ratio of the low-temperature photoresistance signals for the CR-active (CRA) and CR-inactive (CRI) polarities of magnetic field increases with lowering power, but, nevertheless, remains substantially lower than expected from conventional theory assuming interaction of the plane electromagnetic wave with the uniform 2DES. Our analysis shows that all data can be well described by the nonlinear CR-enhanced electron gas heating in both CRA and CRI regimes. This description, however, does not specify the source of anomalous CRI absorption that remains unclear.

I. INTRODUCTION

The electron cyclotron resonance (CR) is one of the central phenomena in magneto-optics, in particular, providing a standard method to measure the energy dispersion of carriers in three-dimensional (3D) and two-dimensional (2D) conducting materials (see, e.g., Refs. [1,2]). The resonance occurs when the frequency of radiation matches that of the cyclotron motion of carriers in a static magnetic field. Importantly, in the Faraday geometry and for the circularly polarized electromagnetic (EM) wave the CR emerges for one magnetic field polarity only. Specifically, the electrons should perform a helical (3D) or circular (2D) motion with the same sense of rotation as the driving force of the EM wave, as only in this case the electric and magnetic forces continuously match. This is called the CR-active (CRA) regime. Consequently, for the opposite polarity of the magnetic field or opposite helicity of the EM wave the CR should be absent, which is usually called the CR-inactive (CRI) regime.

The main experimental approaches to CR studies include all-optical transmission or reflection spectroscopy, the optically detected cyclotron resonance (ODCR), and photoelectric methods (for review see Ref. [2]). The latter, studying the CR photoresistance or photocurrent, are particularly important for exploration of modern 2D materials. Apart from the energy spectrum, the photoelectric methods provide valuable information on elastic and inelastic scattering processes controlling the momentum and energy relaxation. Moreover, such studies provide access to rich spectrum of CR-related nonequilibrium phenomena such as microwave-induced resistance oscillations (MIRO) [3,4], magnetoplasmon effects including excitation of nonlocal Bernstein modes [5], non-Markovian classical memory effects [6], to name a few. Stunningly, recent studies of these effects in 2D electron systems (2DES) revealed up to 100% immunity of the CR response to radiation helicity, first in MIRO studies [7–9] and, most recently, also in the CR photoresistance and photocurrent [10].

In all these experiments, the CR helicity anomaly was detected solely in the photoelectric response, whereas the simultaneous transmittance measurements demonstrated regular strong helicity dependence, in full agreement with the well-established Drude theory of the CR. The anomaly was detected even in 2DES samples with lateral size much larger than the beam spot of the radiation, that excludes depolarization effects due to diffraction on sample edges or contacts as a possible origin of the anomaly.

Here we report on a detailed study of the CR helicity anomaly. Studying the terahertz radiation-induced change of the low-frequency resistance in high-mobility GaAs/AlGaAs quantum well (QW) structures we observed that the ratio of the CR signals in the CRA and CRI regimes (CRA/CRI ratio) crucially depends on the radiation power P. While at high P and low temperatures T the CRA/CRI ratio can be close to unity (100% immunity), it substantially increases at low P and/or high T. Importantly, even at the lowest powers the CRA/CRI ratio remains anomalously low. We demonstrate that the observed power dependence of the CRA/CRI ratio is caused by saturation of the photoresistance which has different saturation powers for the CRA and CRI polarities.

Our analysis shows that, in the CRA regime, both photoelectric response and the magnetotransmittance can be consistently described using the standard theory, with the

*Corresponding author: sergey.ganichev@ur.de

TABLE I. Electron density n_e, mobility μ, and momentum relaxation time τ_p obtained from magnetotransport data at $T = 1.8$ K. Third column indicates whether data were obtained in the dark or after short illumination by room light. Note that in sample No. B such illumination does not lead to essential changes of n_e and μ, but still promotes the visibility of the quantum effects such as SdHO and MIRO.

Sample	Wafer label	QW thickness (nm)	With room light illumination	n_e 10^{11} (cm^{-2})	μ 10^6 (cm^2/Vs)	τ_p (ps)
No. A	C512C	10	no	7	0.37	13
No. A	C512C	10	yes	12	0.66	24
No. B	1614	16	no	7	1	36
No. B	1614	16	yes	7	1	36

nonlinear power dependence caused by uniform electron gas heating by the plane circularly polarized EM wave due to nonlinear energy losses. On the other hand, the observed behavior of the resonant photoresistance in the CRI regime appears to be very similar to that in the CRA regime, but with a smaller overall magnitude and different saturation intensity. Thus, it should be attributed to the same physical mechanisms, but with a weaker CRI resonant absorption in comparison to the CRA regime. While microscopic mechanisms of the anomalous CRI absorption remain unclear, our results suggest that 2DES induces evanescent wave components of opposite helicity with respect to the incoming circularly polarized wave. Most importantly, unlike previous experiments showing complete polarization immunity, the identified nonlinearity of the CRA/CRI ratio shows that, in the linear intensity regime, it is sufficient to clarify the presence of a resonant CRI signal that is several times weaker than the regular CRA signal.

II. SAMPLES AND METHODS

For our study on the CR we used large-sized GaAs-based heterostructures of different quantum well (QW) thicknesses and fabrication. The first (sample No. A) one consists of an AlGaAs/GaAs QW structure with a thickness of 10 nm, while the second one (sample No. B) is made of a selectively doped 16-nm GaAs QW with AlAs/GaAs superlattice barriers, both grown by molecular-beam epitaxy (MBE) on a GaAs substrate. For more information on samples, see Refs. [10,11]. The samples were prepared in a van der Pauw geometry both exhibiting a size of 10×10 mm^2 exceeding the diameter of the spot of the incoming THz or sub-THz beam (see Fig. 1). Ohmic contacts made out of indium and Ge/Au/Ni/Au for the 10-nm and 16-nm GaAs sample, respectively, were applied to the corners. The transport parameters such as electron density and mobility obtained by conventional magnetotransport measurements are collected in Table I. The photoresistance and transmittance experiments were performed on samples in the darkness or after short illumination by room light. The latter leads to a change of transport characteristics due to the persistent photoconductivity effect [12].

As radiation sources we used a tunable continuous-wave (cw) impact ionization avalanche transit time diode (IMPATT diode) based system [13,14], an optically pumped cw molecular gas laser [15,16], and backward-wave oscillators (BWOs) [17]. The former consists of a local oscillator operating at 7.3 to 14.6 GHz and a frequency multiplier chain increasing the frequency by 24 times. The system yields

continuously tunable radiation operating in the range from $f = 0.28$ to 0.312 THz and having a maximum power up to $P = 30$ mW. The molecular laser operates at a frequency of $f = 0.69$ THz providing powers up to $P = 8$ mW. The BWO system provided radiation with $f = 0.35$ THz and a power of $P \sim 0.5$ mW at the sample surface [11].

The CR experiments were performed in a temperature-regulated Oxford Cryomag optical cryostat equipped with z-cut crystal quartz windows, which were covered by black polyethylene films. The films are almost transparent in the THz range, but block uncontrolled illumination by the ambient light. Photoresistance and transmittance measurements were performed in the Faraday geometry with a magnetic field B up to 7 T applied perpendicularly to the QW plane
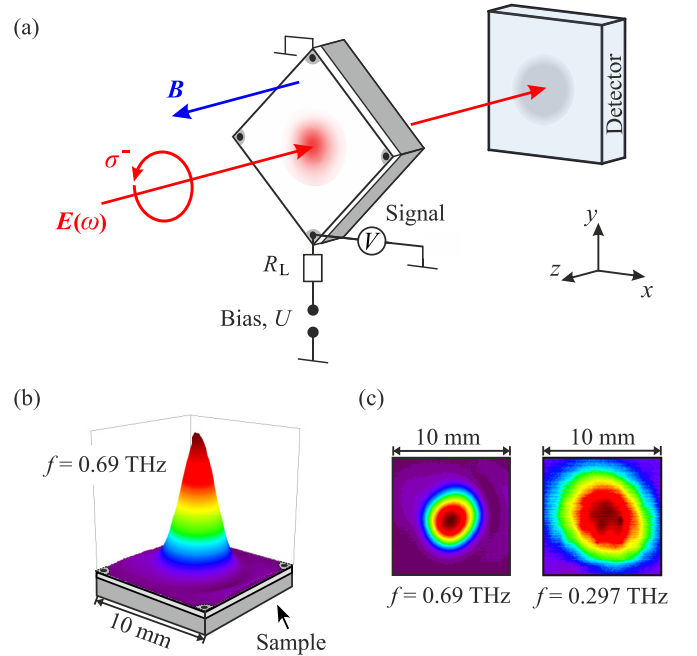

FIG. 1. (a) Sketch of the experimental setup used for simultaneous measurements of the photoresistance and radiation transmittance. Most experiments were performed in the shown two-terminal configuration, apart from several measurements in four-terminal configuration which will be mentioned in the text below. (b) Three-dimensional intensity profile of the laser beam at $f = 0.69$ THz, focused at the 10×10 mm^2 GaAs sample, measured by the pyroelectric camera. (c) Corresponding beam cross sections recorded for $f = 0.69$ and 0.297 THz, plotted using the color scheme of (b). The respective FWHM (full width at half-maximum) spot diameters are $d = 3.0$ and 5.8 mm.

[see Fig. 1(a)]. The sample was illuminated from the top side containing the 2DES by monochromatic THz radiation with frequencies in the range from $f = 0.28$ to 0.69 THz and radiation powers up to $P = 30$ mW. The radiation was focused on the sample by an off-axis parabolic mirror. The intensity distribution and the spot size of the beam were monitored by a pyroelectric camera. Depending on the radiation frequency, the spot diameter d, determined as the full width at half-maximum (FWHM) of the recorded intensity profiles, varied between $d = 3$ and 5.8 mm. For all frequencies it was substantially smaller than the lateral dimensions of the square-shaped samples (10×10 mm^2) [see Fig. 1(b)]. This allowed us to exclude possible contributions from edge and contact illumination in photoresistance and transmittance measurements. Here it is appropriate to mention previous experiments [8] on similar structures using THz laser beams scanning across the edge of the sample. Even in the case of significant illumination of the edges, both photoelectric and transmittance signals there just followed the decrease in radiation power approaching 2DES, with no effect on their helicity dependence. The transmitted radiation was detected by a pyroelectric detector placed behind the sample, simultaneously with the photoresistance measured in two-terminal configuration [see Fig. 1(a)].

In the experiments in Regensburg described below we used left-(σ^-) and right-(σ^+) handed circular polarized radiation. To modify the initial linear polarization state, a waveguide polarizer was directly connected to the radiation output of the IMPATT diode-based system, while the molecular laser setup utilized x-cut crystal quartz quarter wave plates.

Experiments performed in Vienna employed coherent BWO radiation and an optical cryostat with mylar windows covered by black polypropylene plates. A polarization transformer, consisting of a tunable plane mirror placed in parallel to a fixed wire grid polarizer, was used to create the circular polarization [7,11]. The samples were irradiated from the substrate side. The phototransport measurements were performed using the double modulation technique and four-terminal configuration (see [18,19] and Supplemental Material in Ref. [20]). Conditions for reliable polarization-sensitive photoelectric measurements using this setup, including the relation between the sample and beam size, were established in Ref. [11] and are met for the data presented below. Transport measurements performed in Vienna and Regensburg in the absence of THz illumination confirmed that the samples parameters remained the same during measurements in both locations.

To vary the radiation power we used either an internal waveguide attenuator (IMPATT) or a so-called cross-polarizer technique (molecular laser, BWO). The latter consists of two wire grid polarizers, where the rotation of the first one modifies the radiation power, while the second one was fixed to ensure an unchanged output polarization [21,22].

III. RESULTS

Below we present the results of our measurements. We start with the THz photoresistance data obtained in sample No. A without exposure to room light (Sec. III A). Under these conditions the photoresistance is mainly caused by electron gas heating due to radiation absorption at the CR (bolometric response). Next, we describe the results obtained for the same sample, but exposed to ambient light for a short time (Sec. III B). The latter changes the transport characteristics and gives rise to MIRO in the photoresistance. In the same section we present the results obtained in sample No. B after brief illumination by room light.

A. THz response of sample No. A without prior exposure to room light

Figure 2(a) shows the normalized transmitted signal $\mathcal{T}/\mathcal{T}(B = 0)$, recorded at $T = 1.8$ K for sample No. A. It was obtained using the IMPATT diode system operating at a frequency of $f = 0.297$ THz, at the highest available power of $P = 10$ mW and for left-handed circularly polarized radiation (σ^-). The CR (centered at $B = B_{\mathrm{CR}}$, indicated by a vertical dashed line) is clearly visible as a dip at the CRA side, which corresponds to positive B for σ^- polarization. As discussed in more detail in Sec. IV, the shape of the measured transmittance can be well reproduced by standard Drude theory incorporating the effects of strong metallic reflection from high-mobility and high-density 2DES as well as multiple reflections of the plane EM wave within the dielectric substrate (Fabry-Pérot interference) [8,23]. In this particular case, the CR in the transmittance has a relatively narrow width that is caused by destructive interference in the substrate. Importantly, the transmittance is almost flat at the CRI side, i.e., at $B < 0$, including the vicinity of $B = -B_{\mathrm{CR}}$ (dashed line). This ensures a high purity of the polarization state of the transmitted wave and, therefore, also of the incoming wave on the opposite side of the sample.

Figures 2(b) and 3(b) display traces of the photoresistance ΔR_{xx} obtained via varying the radiation power P at fixed temperature $T = 1.8$ K and for various T at fixed $P = 10$ mW, correspondingly. The traces are offset for clarity and normalized to the maximum positive signal on the CRA side to facilitate the comparison. First of all, it is immediately seen that, in sharp contrast to the simultaneously measured transmittance, Figs. 2(a) and 3(a), the resonant response in ΔR_{xx} is detected for both CRA and CRI magnetic field polarities and, quite surprisingly, has similar magnitudes. A quick inspection shows that the shape of the resonant photoresistance appears to be very similar on both sides, whereas the relative magnitude of the CRA and CRI signals is highly sensitive to temperature and radiation power.

On the CRA side, the behavior of ΔR_{xx} is rather ordinary and can be directly attributed to the conventional resonant CR absorption and associated heating of the electron gas by circularly polarized radiation (bolometric effect, see, e.g., Ref. [16] and Sec. IV for details). At high T the photoresistance exhibits a resonant peak [see several upper traces in Fig. 3(b)] that is associated with the heating-induced decrease of the mobility of 2DES (μ photoconductivity [16]). At low T, Figs. 2(b) and 2(c) and lower traces in Fig. 3(b), the electron gas heating primarily leads to resonant suppression of Shubnikov–de Haas oscillations (SdHO), resulting in the emergence of SdHO-periodic sign-alternating oscillations in ΔR_{xx}. Similar to the resonant peak at high T, the envelope of oscillations at low T reflects the B dependence of
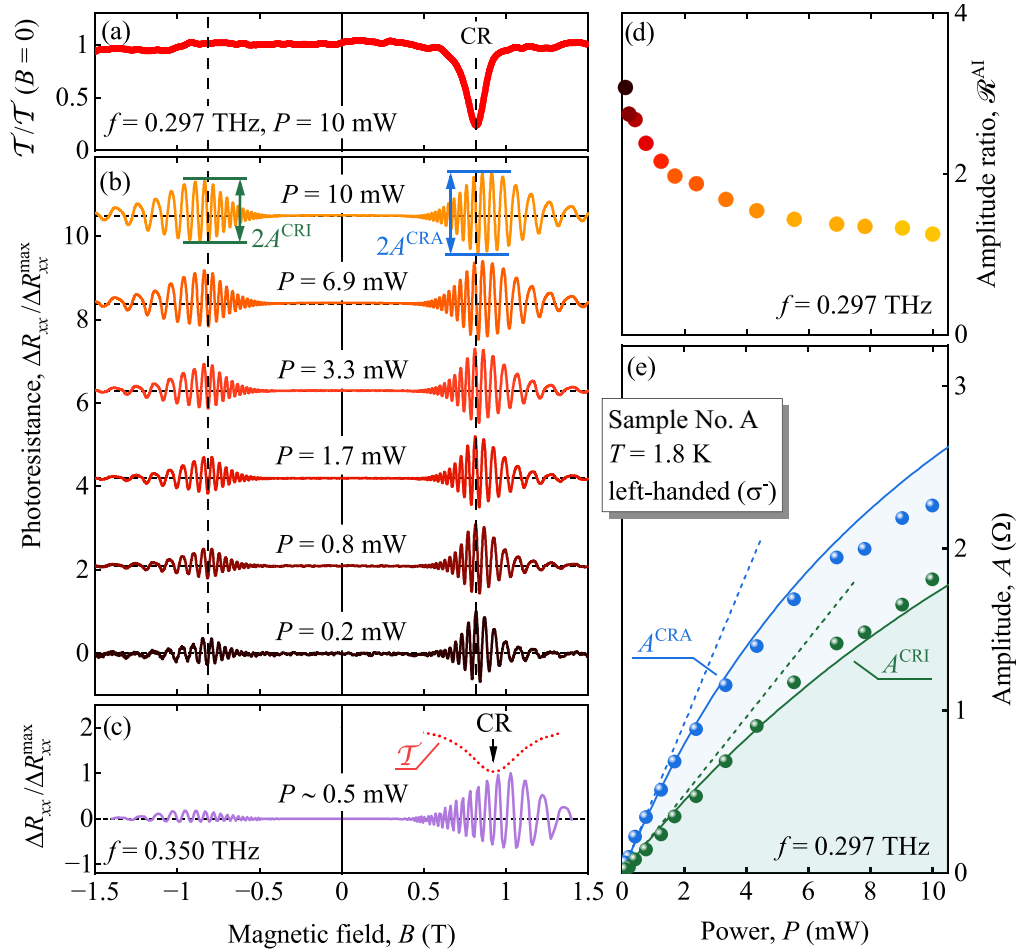
FIG. 2. Results obtained in sample No. A at $T = 1.8$ K without prior room light illumination. (a), (b) Data measured under left-handed circularly polarized radiation (σ^-) produced by the IMPATT diode operating at a frequency $f = 0.297$ THz. (a) Radiation transmittance recorded at radiation power of $P = 10$ mW and normalized to its value at zero magnetic field, $\mathcal{T}/\mathcal{T}(B = 0)$. (b) Photoresistance measured at various radiation powers. The traces are normalized to the signal's maximum $\Delta R_{xx}/\Delta R_{xx}^{\max}$ and are up-shifted for clarity. The vertical dashed line on the right side indicates the position of the CR obtained from the minimum of the transmittance. The left vertical dashed line marks the corresponding CR position for the opposite helicity. The blue and green vertical double arrows illustrate how the amplitudes A^{CRA} and A^{CRI} of the resonant photoresistance signals are determined on the CRA and CRI sides. (c) Photoresistance (purple trace) obtained using BWO operating at $f = 0.350$ THz and $P \simeq 0.5$ mW. The red dotted line shows the corresponding CR dip in the simultaneously measured transmittance. The ratio $\mathcal{R}^{\text{AI}} = A^{\text{CRA}}/A^{\text{CRI}} = 6.5$ in this case was larger than that obtained for $f = 0.297$ THz [see (d)]. (d) Power dependence of the ratio $\mathcal{R}^{\text{AI}} = A^{\text{CRA}}/A^{\text{CRI}}$ of the CRA and CRI amplitudes for the data measured at $f = 0.297$ THz [selected traces are shown in (b)]. (e) Power dependence of A^{CRA} (blue circles) and A^{CRI} (green circles), as extracted from unnormalized photoresistance data ΔR_{xx} measured at $f = 0.297$ THz. Solid lines are calculated according to Eq. (2) using a and P_s as fitting parameters ($a^{\text{CRA}} = 0.46$ Ω/mW and $P_s^{\text{CRA}} = 12.5$ mW at the CRA side, $a^{\text{CRI}} = 0.24$ Ω/mW and $P_s^{\text{CRI}} = 25$ mW at the CRI side). Dashed lines illustrate the linear part $A = aP$ of the corresponding fits.

radiation-induced changes of the electron temperature. At intermediate temperatures the photoresponse is caused by the superposition of the μ-photoconductivity and the suppression of SdHO.

For quantitative analysis of the anomalous relative magnitude of the CRA and CRI signals in Figs. 2(b) and 3(b), we define their amplitudes A^{CRA} and A^{CRI} as the peak height at high T and the maximum value of the envelope of the SdHO-related oscillations at low T and introduce their ratio

$$\mathcal{R}^{\text{AI}} = \frac{A^{\text{CRA}}}{A^{\text{CRI}}}. \tag{1}$$

Figures 2(d) and 3(c) reveal that this ratio depends on the radiation power and on the sample temperature, approaching unity at the highest power and lowest temperature.

We first address the power dependence. It is seen that the ratio substantially increases with lowering the power. Such a behavior indicates that both amplitudes depend nonlinearly but in a distinct way on the radiation power. Indeed, plots of individual amplitudes A^{CRA} and A^{CRI} in Fig. 2(e) show that the CRA response substantially saturates with P while for the CRI response the nonlinearity is weaker. At high power, the observed nonlinearity on both sides can be well fitted using the empirical
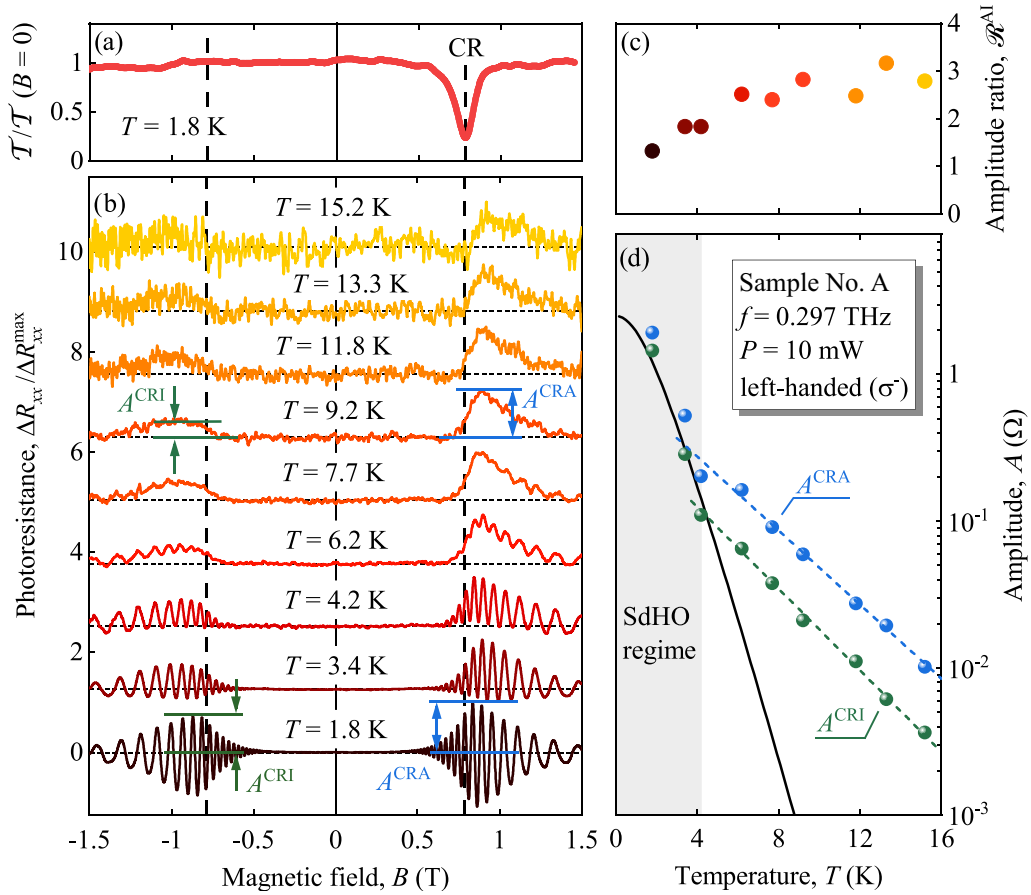
FIG. 3. Results obtained in sample No. A (without prior exposure to room light) under left-handed circularly polarized radiation (σ^-) produced by the IMPATT diode operating at frequency $f = 0.297$ THz with $P = 10$ mW. (a) Radiation transmittance normalized to its value at zero magnetic field $\mathcal{T}/\mathcal{T}(B = 0)$ [same as in Fig. 2(a)]. (b) Normalized photoresistance traces $\Delta R_{xx}/\Delta R_{xx}^{\max}$ at given temperatures from $T = 1.8$ up to 15.2 K. Vertical dashed lines mark the position of the CR for both helicities. Blue and green vertical double arrows (see traces for $T = 1.8$ and 9.2 K) show how the amplitudes A^{CRA} and A^{CRI} are determined from the unnormalized data for ΔR_{xx}. (c) Temperature dependence of the amplitude ratio $\mathscr{R}^{\mathrm{AI}} = A^{\mathrm{CRA}}/A^{\mathrm{CRI}}$. (d) Temperature dependence of individual amplitudes A^{CRA} and A^{CRI}. The gray shaded area marks the interval of $T \leqslant 4.2$ K where the SdHO-periodic oscillations in ΔR_{xx} remain strong. The corresponding solid line is calculated using the Lifshitz-Kosevich formula (see Sec. IV). The dashed blue and green curves serve as guide for the eye, in the region where the SdHO are fully suppressed.

formula

$$A(P) = \frac{aP}{1 + P/P_s}, \qquad (2)$$

with two fitting parameters a and P_s on each side describing the linear behavior at low P and the saturation power, correspondingly. Blue and green curves in Fig. 2(e) show the corresponding fits for A^{CRA} and A^{CRI}. In agreement with the discussion above, these fits show that the saturation power on the CR-active side, $P_s^{\mathrm{CRA}} = 12.5$ mW, is two times smaller than that on the CRI side, $P_s^{\mathrm{CRI}} = 25$ mW. At the same time, the linear coefficients in these fits are $a^{\mathrm{CRA}} = 0.46$ Ω/mW and $a^{\mathrm{CRI}} = 0.24$ Ω/mW, so that their ratios yield $P_s^{\mathrm{CRA}}/P_s^{\mathrm{CRI}} \simeq a^{\mathrm{CRI}}/a^{\mathrm{CRA}}$. It worth mentioning that, while Eq. (2) describes well the nonlinear behavior at high power, at low powers it fails, and the linear regime is not reached even at the lowest power used in our experiments. Correspondingly, the CRA/CRI ratio in Fig. 2(d) does not saturate completely at low P as it should in the linear regime.

As mentioned before, at first glance the shape of the resonant photoresistance for CRA and CRI configurations appears to be very similar. For a closer inspection of this shape and its evolution with P, in Figs. 4(a) and 4(b) we replotted the photoresistance data from Fig. 2(b) without the offset, and with each trace normalized to the corresponding radiation power P. This procedure reveals that the nonlinearity of ΔR_{xx} is pronounced only in the vicinity of $B = B_{\mathrm{CR}}$ in the CRA configuration, Fig. 4(b). It is almost absent in the CRI configuration, as well as at the wings of the CRA signal: here all traces of $\Delta R_{xx}/P$ almost coincide. These observations are in line with the discussion above. Namely, on the CRA side, the electron gas heating is most pronounced at the maximum of CR absorption. At the wings the absorbed power substantially drops and, consequently, the nonlinearity does not show up. At the CRI side, the nonlinearity is weak even at the maximum [see Fig. 2(e)], so the normalized signals $\Delta R_{xx}/P$ behave almost identically at low and high power.

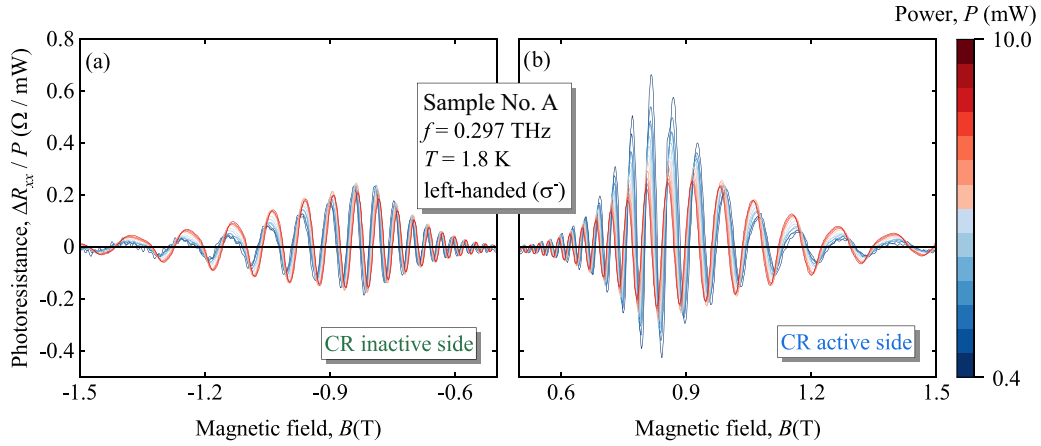In addition to the data obtained at $f = 0.297$ THz, we performed measurements using the BWO setup providing σ^-

FIG. 4. Power dependence of the photoresistance ΔR_{xx} normalized to the radiation power P. Here the same data set as in Fig. 2(b) is used. (a), (b) Resonant photoresponse for CRI and CRA configurations, respectively. The color of individual traces changes from intense blue measured at the lowest ($P = 0.4$ mW) to intense red at the highest power ($P = 10$ mW), as illustrated by the color bar on the right.

radiation at $f = 0.350$ THz and $P \approx 0.5$ mW [see Fig. 2(c)]. In transmittance, the CR dip is also present in the CRA configuration only. Comparing the shape of the dip with that obtained at $f = 0.297$ THz [see Figs. 2(c) and 2(a)], we see that at $f = 0.350$ THz the CR is substantially broader, indicating the constructive Fabry-Pérot interference for this frequency (see Sec. IV and Fig. 8 in the Supplemental Material [24]). The observed ratio $\mathscr{R}^{\text{AI}} = 6.5$ in this case was larger than that obtained for $f = 0.297$ THz [see Fig. 2(d)].

We now turn to the temperature dependence of the ratio $\mathscr{R}^{\text{AI}}$ (see also Ref. [10] as well as Figs. 2 and 4 in the Supplemental Material [24]). Figure 3(c) obtained at $P = 10$ mW shows that it increases with T. The temperature dependencies of the individual amplitudes, A^{CRA} and A^{CRI}, are shown in Fig. 3(d). They reveal that the magnitude of the photoresistance signals on both sides rapidly decreases with growing T. A typical example of the evolution of the shape of the resonant photoresistance with power at higher temperature ($T = 6$ K) is provided in the Supplemental Material [24] (see Fig. 5 there).

The results discussed so far were obtained primarily by applying radiation at $f = 0.297$ THz. Figure 5 demonstrates that the photoresistance in response to radiation of higher frequency, $f = 0.69$ THz, shows a similar behavior. In particular, the ratio $\mathscr{R}^{\text{AI}}$ also increases with the reduction of the radiation power by about 2.5 times [see Fig. 5(c)]. The maximum power at both frequencies was almost the same. However, the spot diameter $d = 3$ mm at $f = 0.69$ THz was substantially smaller than at $f = 0.297$ THz, where $d = 5.8$ mm. Thus, despite the radiation power is similar in both cases, the intensity of $f = 0.69$ THz illumination is about four times higher. While the saturation powers at the CRA side, obtained using the fits according to Eq. (2), are also found to be close to each other at both frequencies [$P_s^{\text{CRA}} = 8.0$ mW at $f = 0.69$ THz vs $P_s^{\text{CRA}} = 12.5$ mW for $f = 0.297$ THz], for CRI configuration the saturation power is substantially reduced at higher f [$P_s^{\text{CRI}} = 16.0$ mW for $f = 0.69$ THz versus $P_s^{\text{CRI}} = 25$ mW for $f = 0.297$ THz]. We mention that also the fitting parameters for the fits in Fig. 5 satisfy the natural relation $P_s^{\text{CRA}}/P_s^{\text{CRI}} \simeq a^{\text{CRI}}/a^{\text{CRA}}$.

B. THz response of samples No. A and No. B after room light illumination

Figure 6 shows the transmittance and photoresistance data measured with the IMPATT diode system on the same sample No. A and with the same radiation frequency $f = 0.297$ THz as in Figs. 2 and 3, but now obtained after brief illumination of the sample with room light prior to the measurements. Such illumination results in a substantial increase of the electron density and mobility due to the persistent photoconductivity effect [12], and also in increase of the quantum lifetime, resulting in emergence of MIRO in the photoresistance [4,8]. The behavior of the transmittance, Fig. 6(a), remains conventional after the room-light illumination: it still reveals a clear CR dip at the CRA configuration only. At the same time, the photoresistance traces, shown in Figs. 6(b) and 6(c), change qualitatively: now we observe additional low-frequency $1/B$-periodic oscillations, in addition to higher-frequency SdHO-related oscillations. The former oscillations are coupled to the harmonics of the CR, yielding nodes at B_{CR} and its harmonics $B_{\text{CR}}/2, B_{\text{CR}}/3, \ldots$ [see thick and thin dashed vertical lines in Figs. 6(b) and 6(c)], the latter indicated for the trace at $P = 6.9$ mW. This behavior is well established for MIRO [3,4]. One observes that, similar to the bolometric photoresistance related to the electron heating, also the amplitudes of MIRO in CRA and CRI configurations are very similar (see also Fig. 6 in the Supplemental Material [24]). For quantitative analysis, we introduce the amplitudes of MIRO, A_M^{CRA} and A_M^{CRI}, as one half of the difference of ΔR_{xx} at maxima and minima around the CR position [see the upper trace in Fig. 6(b)]. The ratio of these amplitudes,

$$\mathscr{R}_M^{\text{AI}} = \frac{A_M^{\text{CRA}}(P)}{A_M^{\text{CRI}}(P)}, \tag{3}$$

is plotted in Fig. 6(d). It is seen that, in contrast to the electron gas heating effects discussed in Sec. III A, the MIRO amplitudes on both sides grow linearly with P [Fig. 6(e)]. Consequently, the CRA/CRI ratio [Eq. (3)] for MIRO is almost independent of the radiation power P [see Fig. 6(d)]. Comparing the absolute values, we see that $\mathscr{R}_M^{\text{AI}}$ is about
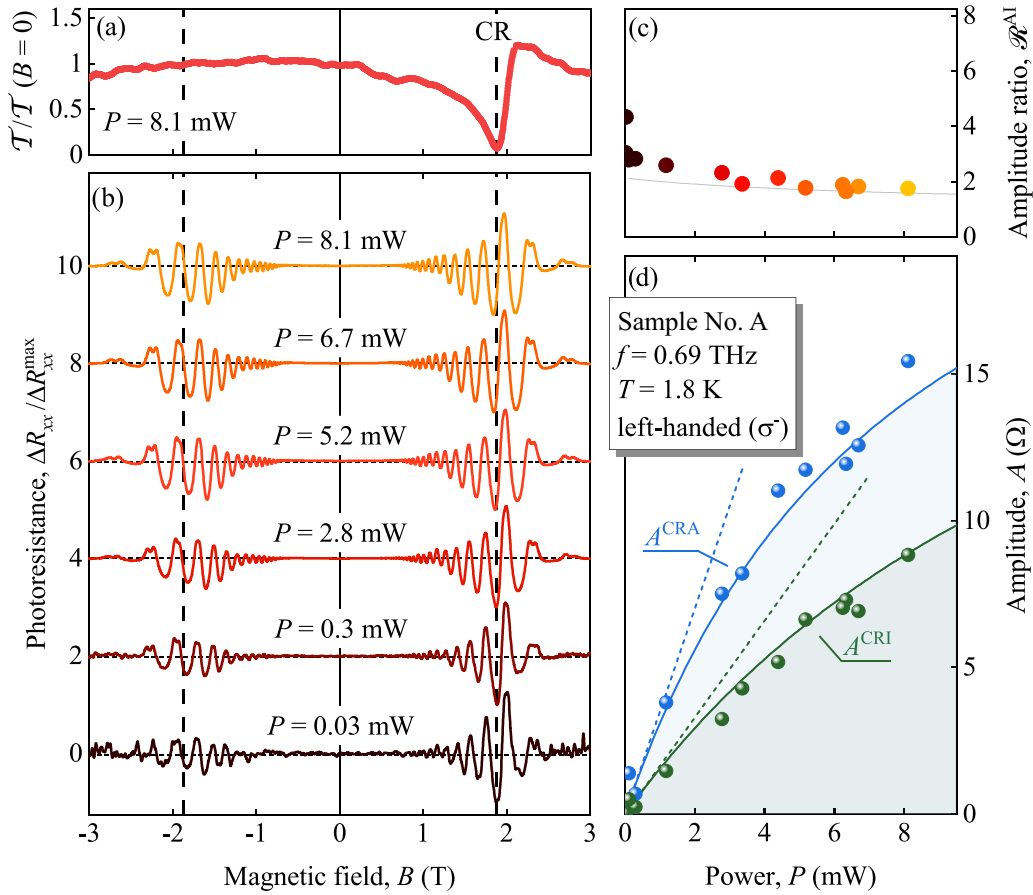
FIG. 5. Results obtained in sample No. A at $T = 1.8$ K without exposure to room light. The data are obtained using left-handed circularly polarized (σ^-) radiation with frequency $f = 0.69$ THz produced by the molecular laser. (a) Normalized transmittance obtained for the highest available power $P = 8.1$ mW. (b) Photoresistance traces measured at various radiation powers. The traces are normalized on the signal's maximum $\Delta R_{xx}/\Delta R_{xx}^{max}$, and are up-shifted for clarity. Vertical dashed lines mark the position of the CR for both helicities. (c) Power dependence of the amplitude ratio $\mathscr{R}^{AI} = A^{CRA}/A^{CRI}$. The amplitudes are obtained as illustrated in Fig. 2. (d) Power dependence of A^{CRA} (blue circles) and A^{CRI} (green circles) extracted from unnormalized photoresistance data. Solid lines are calculated according to Eq. (2) using a and P_s as fitting parameters ($a^{CRA} = 3.51$ Ω/mW and $P_s^{CRA} = 8.0$ mW at the CRA side, $a^{CRI} = 1.64$ Ω/mW and $P_s^{CRI} = 16.0$ mW at the CRI side). Dashed lines illustrate the linear part $A = aP$ of the corresponding fits. The power dependence of the ratio A^{CRA}/A^{CRI} of the fits is illustrated by a solid line in (c).

two times smaller than $\mathscr{R}^{AI}$ detected at the lowest power for the bolometric photoresistance [Fig. 2(d)]. Figure 6(c) presents the traces obtained using the BWO system operating at $f = 0.350$ THz in sample No. A after room-light illumination. Similar to the measurements at this frequency performed without prior illumination by room light [see Fig. 2(c)], also for MIRO the observed ratio $\mathscr{R}_M^{AI}$ is about two times larger than the highest value obtained at $f = 0.297$ THz. While the CRA/CRI ratio in the MIRO-dominated photoresistance is P independent, it increases with T (see Fig. 6 in the Supplemental Material [24]).

Finally, we turn to the description of the results obtained in sample No. B, which features a selectively doped 16-nm GaAs QW with AlAs/GaAs superlattice barriers. Figure 7 shows the transmittance and photoresistance data recorded in response to σ^+ polarized radiation in this sample (illuminated by room light prior to the measurements). As before, the transmittance curve shows a clear transmittance dip in the CRA configuration and no resonant features for the opposite magnetic field polarity. A high asymmetry of the CR dip is caused by the

interference effects (see Sec. IV). The photoresistance traces at different P are shown for two temperatures in Figs. 7(b) and 7(d). At low temperature, $T = 1.8$ K, the photoresistance displays MIRO modulating high-frequency SdHO-related oscillations [see Fig. 7(b)]. An increase of the measurement temperature results in full suppression of SdHO and in a significant suppression of MIRO. At $T = 18$ K [Fig. 7(d)], the photoresistance is dominated by the resonant electron heating that reduces the mobility and produces the corresponding single CR peak in the photoresistance. Figure 7(c) shows that at all T the ratio $\mathscr{R}_M^{AI}$ does not appreciably change with P, similar to the behavior detected in sample No. A [see Fig. 6(d)]. Also similar to sample No. A, the ratio of the CRA and CRI signals increases at higher T (see also Fig. 7 in the Supplemental Material [24]).

IV. DISCUSSION

Our experiments reveal that the low-temperature photoresistance of 2DES in response to circularly polarized radiation
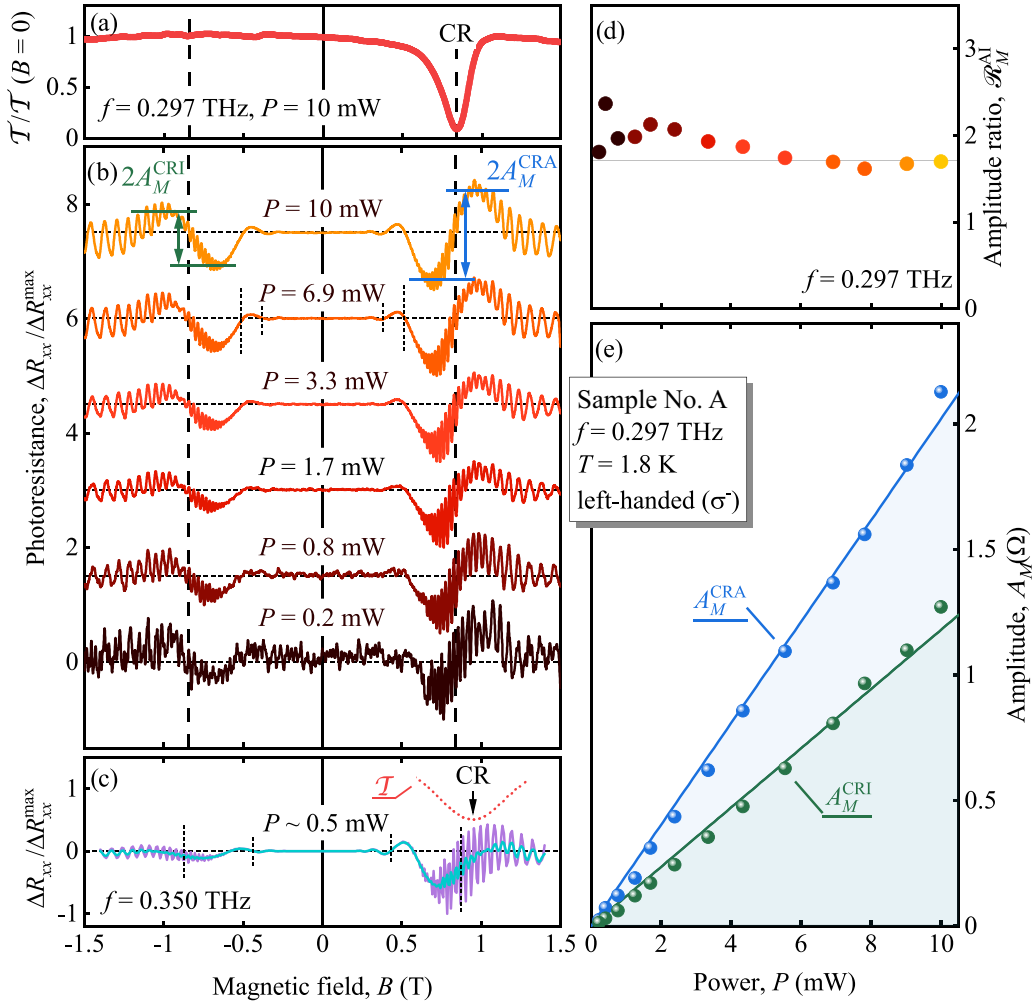
FIG. 6. Results obtained at $T = 1.8$ K on sample No. A after prior exposure to room light. (a), (b), (e) Data measured under left-handed circularly polarized radiation (σ^-) produced by the IMPATT diode operating at frequency $f = 0.297$ THz. (a) Radiation transmittance recorded at radiation power of $P = 10$ mW and normalized to its value at zero magnetic field $\mathcal{T}/\mathcal{T}(B = 0)$. (b) Photoresistance measured at various radiation powers. The traces are normalized to the signal's maximum $\Delta R_{xx}/\Delta R_{xx}^{\max}$ and are up-shifted for clarity. Vertical dashed lines mark the CR position for both helicities. The blue and green vertical double arrows illustrate how MIRO amplitudes, A_M^{CRA} and A_M^{CRI}, are determined on the CRA and CRI sides. Thinner dashed vertical lines, shown as an example for the trace at $P = 6.9$ mW, indicate the second, $\pm B_{\mathrm{CR}}/2$, and third, $\pm B_{\mathrm{CR}}/3$, harmonics of the CR corresponding to the nodes of MIRO. (c) Photoresistance (purple trace) obtained using BWO operating at $f = 0.350$ THz and $P \simeq 0.5$ mW after exposing the sample to room light. The cyan trace depicts the photoresistance smoothed by using moving average. The red dotted curve shows the CR dip in the simultaneously measured transmittance. (d) Power dependence of the ratio $\mathscr{R}_M^{\mathrm{AI}} = A_M^{\mathrm{CRA}}/A_M^{\mathrm{CRI}}$ of MIRO amplitudes. The circles refer to the data measured at $f = 0.297$ THz [selected traces are shown in (b)], whereas the purple star represents the photoresistance measured at $f = 0.350$ THz [(c)]. (e) Power dependence of A_M^{CRA} (blue circles) and A_M^{CRI} (green circles). Solid lines are linear fits. Solid line in (d) shows the corresponding constant ratio $\mathscr{R}_M^{\mathrm{AI}}$.

may exhibit almost symmetric CR signals at both polarities of magnetic field B, instead of expected single CR at a positive or negative magnetic field, depending on helicity of the incoming wave. In this work, we find that the anomalous relative amplitude of the photoresistance signals for CR-active and -inactive polarities of B, the ratio $\mathscr{R}^{\mathrm{AI}} = A^{\mathrm{CRA}}/A^{\mathrm{CRI}}$ introduced in Eq. (1), is highly sensitive to both radiation power and temperature (see Figs. 2, and 3, 5, 7, also supported by additional data in the Supplemental Material [24]). While the CRI response in the photoresistance is anomalous, the simultaneously measured transmittance displays an ordinary behavior with a single CR dip. Furthermore, the photoresistance on the CRA side can be pretty well captured by rather common and well-established

mechanisms related to the electron gas heating [16] and MIRO [4].

Therefore, in the analysis below, we first review such conventional behavior of the transmittance and photoresistance under a uniform circularly polarized wave in terms of the local dynamic and static conductivity of a uniform isotropic 2DES. This will include electrodynamic effects, such as CR reflection, absorption, and transmittance of a high-mobility 2DES in Faraday geometry in the presence of the Fabry-Pérot interference in the substrate, and electron heating effects in the photoresistance. The latter should be distinguished in the classical regime of μ-photoconductivity (hot electron bolometer) and in the quantum regimes of SdHO and MIRO, as well as in the linear and nonlinear regimes with respect to radiation
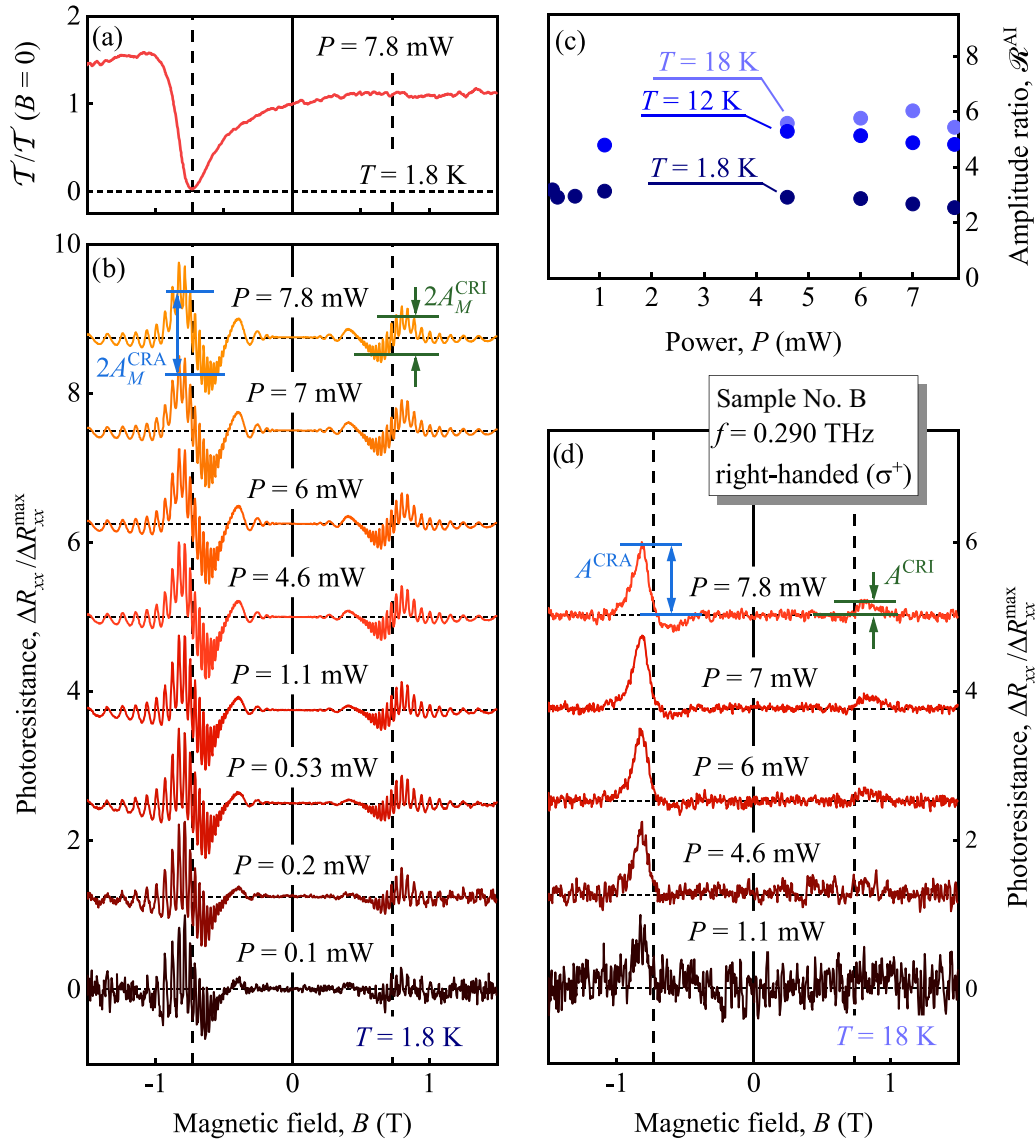
FIG. 7. Results obtained on sample No. B after exposing it to room light and using right-handed circularly polarized radiation (σ^+) produced by the IMPATT diode operating at frequency $f = 0.290$ THz. (a) Radiation transmittance recorded at radiation power of $P = 7.8$ mW and normalized to its value at zero magnetic field $\mathcal{T}/\mathcal{T}(B = 0)$. (b), (d) Photoresistance traces measured at $T = 1.8$ and 18 K, correspondingly, and various radiation powers. The traces are normalized to the signal's maximum $\Delta R_{xx}/\Delta R_{xx}^{\max}$ and are up-shifted for clarity. Vertical dashed lines mark the CR position for both helicities. Blue and green vertical double arrows illustrate how the amplitudes are determined on the CRA and CRI sides at different T (see traces for $P = 7.8$ mW at $T = 1.8$ and 18 K). (c) Power dependence of the ratios $\mathscr{R}_M^{\mathrm{AI}} = A_M^{\mathrm{CRA}}/A_M^{\mathrm{CRI}}$ of MIRO amplitudes at $T = 1.8$ K (dark blue) and power dependencies of the ratios $\mathscr{R}^{\mathrm{AI}} = A^{\mathrm{CRA}}/A^{\mathrm{CRI}}$ of CRA and CRI peak amplitudes at $T = 12$ K (blue) and $T = 18$ K (light blue).

power. Application of this theory to the regular transmittance and to the photoresistance on the CRA side in our experiments allows us to estimate the expected ratio $\mathscr{R}^{\mathrm{AI}}$ (thus providing a quantitative description of the helicity anomaly) and to analyze the observed power dependence of $\mathscr{R}^{\mathrm{AI}}$. After that we discuss possible microscopic origins of the helicity anomaly.

A. CR transmittance, absorptance, and reflectance of a high-mobility 2DES

For a normal incidence of a circularly polarized monochromatic wave to the surface of a sample, containing a 2DES and placed in a perpendicular magnetic field $\boldsymbol{B} = B_z$ (Faraday

geometry), the transmittance $\mathcal{T}(B)$ is given by the standard expression $\mathcal{T}(B) = 4/|s_1(1 + Z_0\sigma_\eta) + s_2|^2$ [4,20,23,25,26]. Here $\sigma_\eta = \sigma_{xx} + i\eta\sigma_{yx}$ is the complex dynamic conductivity of a uniform isotropic 2DES, $\eta = \pm 1$ denotes the helicity of the wave, $Z_0 \approx 377$ Ω is the impedance of the free space, and the complex parameters $s_{1,2} = \cos\phi - in_r^{\mp 1}\sin\phi$ describe the Fabry-Pérot interference due to multiple reflections in the GaAs substrate. The interference phase $2\phi = 4\pi w/\lambda_r$ is given by the ratio of the sample thickness w and the wavelength $\lambda_r = c/fn_r$, where $n_r \simeq 3.6$ is the refractive index of the GaAs substrate. With σ_η taken in the classical Drude form $\sigma_\eta^{\mathrm{D}} = en_e/(\mu^{-1} - iB_{\mathrm{CR}} + i\eta B)$, where $B_{\mathrm{CR}} = 2\pi f m_{\mathrm{CR}}/e$ denotes the position of the CR, the
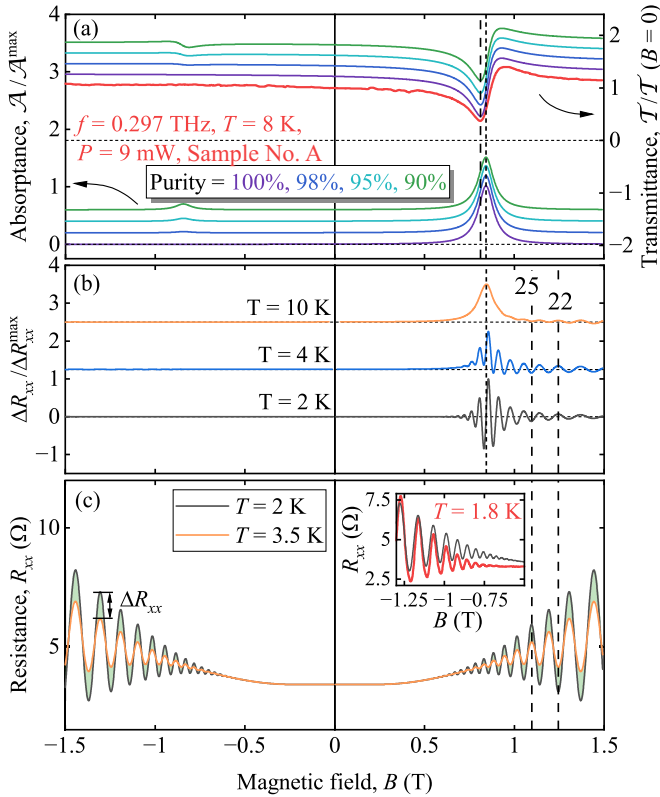
FIG. 8. (a) Drude transmittance $\mathcal{T}^{D}(B)$ and absorptance $\mathcal{A}^{D}(B)$ calculated using Eqs. (4) and (5), with parameters $B_{CR} = 0.82$ T and $\beta = 0.023 - i0.023$ T determined from the transmittance measured at $f = 0.297$ THz, $T = 8$ K, $P = 9$ mW on sample No. A (red). Theoretical curves, calculated for the circular polarization purity of 100%, 98%, 95%, and 90% (bottom to top) are shifted by a constant offset for better visibility. Minimum of transmittance at B_{CR} and maximum of absorptance at $B_{CR} - \mathrm{Im}\beta$ are marked by vertical dashed lines. (b) Normalized photoresistance $\Delta R_{xx}/\Delta R_{xx}^{\max}$ calculated according to Eqs. (8) and (9) for $T = 2$, 4, and 10 K. (c) Dark magnetoresistance $R_{xx}(B)$, calculated using Eq. (9) for $T = 2$ and 3.5 K. Vertical dashed lines in (b) and (c) at filling factors $\nu = 22$ and 25 illustrate the relative phase of SdHO in photoresistance and dark magnetoresistance. Inset in (c) shows measured (red) and calculated (black) magnetoresistance for sample No. A and $T = 1.8$ K. The fit yields parameters $R_0 = 3.4$ Ω, $\tau_q = 1.3$ ps, and $B_{inh} = 1.1$ T used for calculations in (b) and (c).

resulting Drude transmittance $\mathcal{T}^{D}$ and corresponding Drude absorptance $\mathcal{A}^{D} = Z_0 \mathcal{T}^{D} \mathrm{Re}\, \sigma_\eta^{D}$ are given by

$$\mathcal{T}^{D}(B) = |\alpha|^2 \left| 1 - \frac{\beta}{\mu^{-1} + \beta - iB_{CR} + i\eta B} \right|^2, \quad (4)$$

$$\mathcal{A}^{D}(B) = \frac{Z_0 |\alpha|^2 e n_e / \mu}{|\mu^{-1} + \beta - iB_{CR} + i\eta B|^2}. \quad (5)$$

Here $\alpha = 2/(s_1 + s_2)$ and $\beta = e n_e Z_0/(1 + s_2/s_1)$. In the case of illumination of the sample from the 2DES side, as in Figs. 2(c) and 6(c), the expression (5) for $\mathcal{A}^{D}$ should be additionally multiplied by the factor $|s_1|^2$.

Typical shapes of normalized $\mathcal{T}^{D}(B)$ and corresponding $\mathcal{A}^{D}(B)$, calculated according to Eqs. (4) and (5), are shown in Fig. 8(a) together with the experimental transmittance trace

(red line) recorded at $f = 0.297$ THz, $T = 8$ K, and $P = 9$ mW on sample No. A, without prior exposure to room light. The shape of measured $\mathcal{T}(B)$ is well reproduced using $\eta = 1$, corresponding to the left-handed circularly polarized radiation (σ^-), the transport CR width $\mu^{-1} = 0.03$ T obtained using μ extracted from magnetotransport measurements (see Table I), the CR position $B_{CR} = 0.82$ T corresponding to the cyclotron mass $m_{CR} = 0.07 m_0$, and with $\beta = 0.023 - i0.023$ T. The latter parameter accounts for strong metallic reflection from 2DES (superradiant decay [27]), modified by the Fabry-Pérot interference [20], and will be addressed in more detail below.

Most importantly, the conventional Drude theory combined with Maxwell equations accurately reproduces the observed shape of the transmittance for 100% σ^- radiation, confirming the purity of circular polarization in the transmitted, and, thus, also in the incoming wave. For comparison, in Fig. 8(a) we also plot $\mathcal{T}^{D}(B)$ for a plane wave with small admixtures (2%, 5%, and 10%) of σ^+ circular component. It is seen that even a few percent admixture is clearly visible in the transmittance on the CR-passive side $B < 0$. On the other hand, the measured transmittance data do not show any traces of such admixture above the noise level (see also Figs. 2, 3–7, and Supplemental Material [24]). These observations provide a clear evidence that the anomalous CRI signals observed in the photoresistance cannot originate from an admixture of the opposite helicity components in the incoming wave.

A more detailed inspection of the transmittance traces shows that their shape and width vary significantly with the radiation frequency. These modifications mainly come from variations of the Fabry-Pérot interference parameters $s_{1,2}$ which rapidly change with the radiation frequency. In particular, both for constructive ($s_{1,2} = \cos\phi = 1$) and destructive ($\sin\phi = 1$, $s_{1,2} = -i n_r^{\mp 1} \simeq -i3.6^{\mp 1}$) Fabry-Pérot interference the CR dip in the transmittance has a symmetric form, but in the latter case the parameter $\mathrm{Re}[\beta] = \mathrm{Re}[e n_e Z_0/(1 + s_2/s_1)]$ defining the radiative width of the CR is about 14 times smaller. For sample No. A without prior exposure to room light (the electron density $n_e = 7 \times 10^{11}$ cm^{-2}, see Table I), one obtains $\beta = 0.21$ T for constructive and $\beta = 0.015$ T for destructive interference. This substantial difference of the CR width can be seen, for instance, in the transmittance traces presented in Fig. 2(a) (destructive interference) and Fig. 2(c) (constructive interference), obtained on the same sample at different frequencies. Furthermore, as illustrated in Fig. 8(a), intermediate values of the interference phase (corresponding to $\mathrm{Im}\beta \neq 0$) give rise to an asymmetric shape of the transmittance and a corresponding shift of the maximum of the absorptance (dashed lines). Such asymmetric shape of the measured $\mathcal{T}(B)$ is also seen, e.g., in Figs. 5(a) and 7(a) (see also Fig. 8 in the Supplemental Material [24]). As follows from Eqs. (4) and (5), these changes are controlled by the imaginary part of the interference parameter β. In contrast to $\mathcal{T}(B)$, the shape of the Drude absorption remains Lorentzian for all values of β.

Using Eq. (5), we can estimate the expected Drude CRA/CRI ratio of the absorbed power, assuming the 100% circularly polarized radiation that remains uniform in the plane of the 2DES. Taking for definiteness the case of helicity $\eta = 1$, to obtain this ratio we should relate the value of absorptance at the maximum of the Lorentzian

$B = B_{CR} - \text{Im}\beta$ (CRA), to its value at the opposite magnetic field (CRI). Since the CR width is maximal for the condition of constructive interference, the minimal CRA/CRI ratio for the Drude absorption can be estimated as

$$\mathscr{R}_{min}^{AI} = \frac{(\mu^{-1} + \beta)^2 + 4B_{CR}^2}{(\mu^{-1} + \beta)^2} \simeq 47, \qquad (6)$$

where we used the values $\mu^{-1} = 0.03$ T, $B_{CR} = 0.82$ T, and $\beta = 0.21$ T quoted above. At different conditions the ratio can be much larger, for example, for destructive interference, $\beta = 0.015$ T, one obtains $\mathscr{R}_{max}^{AI} \simeq 1330$.

Importantly, these values were estimated for 100% circular polarization, in which case one does not expect any resonant absorption in the CRI regime [see Fig. 8(a)], in contrast to our findings for the photoresistance, where strong *resonant* CRI features are observed. This suggests that in reality the electromagnetic field acting on the 2DES is not a circularly polarized uniform plane wave. On the other hand, as we have seen, the transmittance data provide a clear evidence that the purity of circular polarization in both incoming and transmitted waves is rather high. The estimate (6) and Fig. 8(a) show that in our samples a several percent admixture of the wave with opposite helicity should lead to a similarly weak CRI signal in the photoresistance, also not exceeding several percent of the CRA signal. Before addressing possible mechanisms of the helicity anomalies, we now shortly review the well-established links between the CR absorptance and photoresistance in a uniform EM field which, in particular, explain the observed nonlinear effects in the photoresistance.

B. Electron transport and photoresistance due to electron heating effects

At the CRA side, photoresistance traces (see Figs. 2, and 3, 5) display the well-established behavior associated with resonant electron gas heating under the CR absorption. Under continuous illumination, the heating effects are quite generally described using the energy balance equation

$$\mathcal{A}(I)I = Q(I), \qquad (7)$$

which expresses the stationary condition that the radiation energy $\mathcal{A}(I)I$ absorbed by electrons is fully compensated by the energy flow $Q(I)$ from hot electrons to the lattice [16,28]. The lattice serves as a thermal bath and can be usually assumed to remain at the measurement temperature T. As discussed below, in general both the absorptance $\mathcal{A}$ and losses Q depend on the intensity I of incoming radiation. Importantly, at low electron temperatures, corresponding to conditions of our experiments, the equilibration of the absorbed radiation energy within the electron system, governed by the inelastic electron-electron scattering, is much faster than the rate of energy transfer to the lattice. Therefore, the stationary nonequilibrium energy distribution of electrons under continuous illumination still has the shape of equilibrium Fermi-Dirac distribution, but with the measurement temperature T replaced by an elevated electron temperature $T_e > T$. On the other hand, the heating-induced changes of the chemical potential in a degenerate high-density 2DES can be safely ignored. Thus, the electron temperature T_e is well defined and fully characterizes the electron gas heating effects. The

value of T_e should be found self-consistently from the energy balance equation (7).

In the simplest case of linear heating, corresponding to the limit of low $I \to 0$, one replaces $\mathcal{A}(I)$ with the I-independent linear-response absorptance $\mathcal{A}(I \to 0)$, given in our case by Eq. (5). In turn, the energy losses Q can be rewritten as $(T_e - T)\tau_{e\text{-ph}}^{-1}$, where $\tau_{e\text{-ph}}^{-1}(T_e, T)$ characterizes the electron-phonon energy relaxation rate. Therefore, in the linear heating regime $T_e - T \propto I \mathcal{A}^D(B)\tau_{e\text{-ph}}(T, T)$, where only the absorption rate essentially depends on B. Note that in the linear regime $(T_e - T)/T \propto I \to 0$ the inelastic relaxation rate $\tau_{e\text{-ph}}^{-1}(T_e, T)$, that is usually strongly temperature dependent, and, in general, depends in a distinct way on electron and lattice temperatures, should be replaced by the intensity-independent rate $\tau_{e\text{-ph}}^{-1}(T, T)$. In turn, the photoresistance due to electron heating in the linear regime is given by

$$\Delta R = \frac{\partial R}{\partial T_e}(T_e - T). \qquad (8)$$

The dependence of the resistance $R(T_e, T)$ on the electron and lattice temperature is also in general different, so it may be not sufficient to measure the T dependence of dark resistance to determine the coefficient $\partial R/\partial T_e$.

As outlined above in Sec. III A, in our experiments the electron heating produces a combination of two distinct effects in the photoresistance. Namely, at high T we observe a single CR peak in ΔR caused by heating-induced decrease of the electron mobility [16,29–34], while at the lowest T the main effect of the resonant electron heating comes from the reduction of the SdHO amplitude reflecting their exponential sensitivity to the electron temperature T_e.

In the high-T regime where the SdHO are absent, the longitudinal resistance is B independent and is given by the Drude expression $R_0 = g/(en_e\mu)$, where g is a geometrical factor depending on the type of measurements. According to Eq. (8), in this case the B dependence of the linear photoresistance $\Delta R \propto -I(\partial\mu/\partial T_e)\mathcal{A}^D(B)$ should directly reproduce the Lorentzian shape of the magnetoabsorptance [see Eq. (5)] illustrated in Fig. 8(a). Our observations in the CRA regime at high T are well captured by this mechanism termed μ-photoconductivity (see high-T traces in Fig. 3). The positive sign of ΔR is consistent with the decrease of mobility at high T_e due to acoustic phonon scattering. We emphasize that so far we are discussing the linear regime of weak heating $\Delta R \propto I$. The nonlinear effects will be considered in the next subsection.

At lower T, one should account for the combined effect of CR heating on the mobility and SdHO, as illustrated in Figs. 8(b) and 8(c). In Fig. 8(c), the calculated resistance in the absence of radiation is shown for two temperatures, $T = 2$ and 3.5 K. Here we use standard Lifshitz-Kosevich formula for SdHO [4,35,36],

$$R_{xx}(B) = R_0 + 2R_0\delta^2 - 4R_0\delta_{inh}\delta\frac{X(T)}{\sinh X(T)}\cos(\pi\nu). \qquad (9)$$

The SdHO, described by the last term, are $1/B$-periodic oscillations caused by the modulation of the density of states, and their period is controlled by the carrier density

n_e (the filling factor $\nu = 2\pi\hbar n_e/e|B|$). At zero temperature $T = 0$, the decay of SdHO at low B is described by the Dingle factor $\delta = \exp(-\pi/\omega_c\tau_q)$, where the quantum relaxation time τ_q characterizes the disorder broadening of Landau levels separated by $\hbar\omega_c = \hbar e|B|/m$. The factor containing $X(T) = 2\pi^2 k_B T_e/\hbar\omega_c$ accounts for the additional T smearing. For generality, in Eq. (9) we also include the nonoscillating quantum correction $2R_0\delta^2$ and an additional damping factor $\delta_{\text{inh}} = \exp(-B_{\text{inh}}^2/B^2)$, accounting for possible smooth fluctuations of the filling factor across the sample [4]. In Fig. 8(c), the parameters entering Eq. (9) (see caption) are chosen such that the calculated R_{xx} closely reproduces the experimental magnetoresistance, as illustrated in the inset.

Using Eq. (9) with the chosen parameters together with Eq. (8), in Fig. 8(b) we illustrate the corresponding changes of the photoresistance behavior with the measurement temperature at low intensities. It is seen that the photoresistance oscillations exhibit maxima (minima) at even (odd) Landau-level filling factors, unlike SdHO in the dark magnetotransport having minima (maxima) at even (odd) filling factors [see dashed lines in Figs. 8(b) and 8(c)]. This behavior is well reproduced in our photoresistance data for all samples in conditions where the SdHO-related heating mechanism dominates, and corresponds to the expected reduction of the oscillation amplitude due to heating. At $T = 2$ K, the SdHO-related contribution to the photoresistance in Fig. 8(b) dominates and the oscillations are symmetric with respect to $\Delta R = 0$; the envelope is distorted from the Lorentzian shape due to the exponential decay of SdHO at low B. At higher temperatures, $T = 4$ and 10 K in Fig. 8(b), the SdHO get gradually suppressed, and the nonoscillating contribution related to μ-photoconductivity takes over. This leads to the Lorentzian shape of the photoresistance reproducing that of the magnetoabsorption. All these general features are clearly seen in our photoresistance traces [see Figs. 2(b) and 2(c), 3(b), and 5(b)].

C. Nonlinearity in CRA

Our experiments reveal that the increase of the radiation intensity leads to a sublinear power dependence of the photoresistance [see, e.g., Figs. 2(e) and 5(d)]. We attribute these changes to the nonlinear electron heating. In general, the nonlinearity of $T_e(I)$ can be caused by the saturation of the radiation absorption $\mathcal{A}(I)$ and/or the nonlinearity of energy losses $Q(I)$ [see Eq. (7)]. The former usually becomes essential at very high intensities $I \gtrsim 100$ kW/cm^2 [22,37–39] and thus plays no role here. By contrast, the nonlinear dependence of the rate of energy losses $Q(I)$ becomes essential at much lower powers, as soon as the heating $T_e - T$ is no longer much smaller than T. One of the best-known examples of such nonlinearity is the case of low-angle electron-phonon scattering which was considered theoretically in Ref. [28] and observed in saturation of THz photoresistance in Si-MOSFET structures [16,40,41]. At the lowest T, the dependence $Q \propto T_e^5 - T^5$ is very strong, resulting in fast growth of energy losses with increasing I, and, consequently, to sublinear growth (saturation) of the electron temperature T_e. At higher T, the dependence usually becomes weaker, and saturation takes

place at higher intensities. Finally, at very high T, the universal regime of $Q \propto T_e - T$, characterized by equal thermal occupation of all involved phonon modes, is reached. In this case, the nonlinearity of the energy losses is absent even at high I, and possible nonlinearities of the photoresistance are governed by other mechanisms.[1]

In addition to the above considerations, the basic requirement for the nonlinearity of the electron heating is that the resulting $(T_e - T)/T$ is not too small. The higher is the measurement temperature, the higher radiation intensity is required to fulfill this condition. The degree of electron heating can be estimated from transport data and calculations presented in Fig. 8(c) after being compared to the absolute values of the measured photoresistance. We find that the electron temperature change is comparable to the measurement temperature for the highest intensities and lowest measurement temperature of 2 K. This is consistent with considerable nonlinearity of the electron heating observed in this regime on the CRA side (see Figs. 2 and 5). At sufficiently low intensities and/or high measurement temperatures the heating becomes weak, and no nonlinearity is expected. This agrees well with our observations at high T showing no saturation and, correspondingly, no essential changes of the CRA/CRI ratio with the radiation intensity (see Supplemental Material [24]).

Apart from the sublinear growth of the magnitude of resonant photoresistance signals with intensity, clearly seen in Figs. 2(e) and 5(d), the nonlinear electron heating naturally leads to an additional broadening of these signals. Indeed, collecting the photoresistance signals obtained at different intensities and normalizing them to the radiation power, in Fig. 4 we reveal the strongest saturation near the maxima of the CRA signals, corresponding to the maximal absorption and electron heating. By contrast, both at the wings of the CRA signals and on the CRI side the electron heating remains almost linear even at the highest I. This explains the observed increase of the CRA/CRI ratio [Eq. (1)] at low intensities as a result of a transition from the nonlinear to the linear electron heating regime. However, even at the lowest I available for our measurements this ratio remains anomalously low [see Figs. 2(d) and 5(c)]. The situation becomes different at higher T, as illustrated by a similar analysis of the shape of the photoresistance at $T = 6$ K (see Fig. 5 in the Supplemental Material [24]). As discussed above, at higher T the nonlinear heating effects become weaker. Accordingly, the shape of the CR photoresistance and, therefore, also the CRA/CRI ratio at high T do not appreciably change within the available range of radiation power (see also Fig. 4 in the Supplemental Material [24]).

---

[1]Apart from saturation of the radiation absorption $\mathcal{A}(I)$ mentioned above, these can result from details of the temperature dependence of resistance $R(T_e, T)$, which can be governed by different microscopic mechanisms in different temperature regimes. In other words, at high I, Eq. (8) is not always applicable, and should be replaced by a more general expression for the photoresistance $\Delta R = R[T_e(I), T] - R[T_e(I \to 0), T]$.

D. CRI photoresistance and nature of the anomalous CRI absorption

The discussion above demonstrates that both transmittance and photoresistance data obtained in the CRA regime are conventional and are well described by the standard theory. At the same time, the strength of the detected CRI signals in the photoresistance is clearly anomalous. Taking into account the very similar shape and comparable magnitude of CRA and CRI signals [see Figs. 2(b) and 2(c), 3(b), and 5(b)], the whole photoresistance data could be readily explained assuming them as a response to elliptical, and sometimes, almost linearly polarized radiation. This, however, contradicts the measured transmittance [Figs. 2(a) and 2(c), 3(a), and 5(a)], which unambiguously demonstrates a high purity of the incoming circularly polarized radiation.

The central assumption underlying this apparent paradox is that conventional theory of the CR in transmittance, absorptance, and photoresistance considers a uniform local current response of 2DES to the electric field of a uniform plane circularly polarized wave [4,11]. Such response is fully encoded in the local dynamic conductivity, and becomes resonant at positive or negative B only, depending on the helicity of the incoming wave. It is clear that this standard and widely employed theory is incompatible with the observed anomalously strong CRI absorption.

That is why in Ref. [10] it was proposed that the helicity anomalies may originate from conversion of the uniform THz radiation into nonuniform evanescent near fields, which are present only in a close vicinity of the 2DES and are accompanied by the emergence of spatially nonuniform electric currents there. Unlike the uniform field of the incoming plane wave, nonuniform near fields couple to longitudinal plasmonic excitations and, by their nature, cannot be circularly polarized. Therefore, the polarization state of the total THz field is inevitably altered and is different from that of the incoming wave. In particular, the scattered components of the wave can indeed produce similar CRA and CRI signals in the photoresistance, superimposed on the regular CRA response from the plane-wave component. Within this scenario, the controversy between the helicity dependence of measured transmittance and photoresistance is immediately resolved. Indeed, the magnetotransmittance is measured in the far field, and thus its shape cannot be affected by near-field effects as long as the far-to-near-field conversion depends weakly on the applied magnetic field. In contrast, the absorption by the 2DES and, consequently, the photoresistance are sensitive to the total local field including both far- and near-field components.

It is quite remarkable that the detected CRA and CRI signals in the photoresistance turn out to be comparable in magnitude despite high quality and uniformity of the studied 2DES. Indeed, usually the near-field effects are considered to arise due to a presence of macroscopic metallic objects [42–44] while in present experiments we deal with a nominally uniform 2DES with the size much larger than the laser spot where strong near-field effects are usually not expected to occur. However, it should be taken into account that a significant part of the incoming radiation on the CRA side is reflected from the 2DES. This metallic reflection strongly suppresses the plane-wave component reaching the 2DES at

the regular CR and, therefore, also the scattered near fields emerging on the CRA side. By contrast, on the CRI side the circularly polarized plane wave is almost fully transmitted. Thus, the generated near fields in the CRI regime can be substantially stronger than on the CRA side.

At the same time, the microscopic origin of the near fields in the nominally uniform systems we study remains unknown. In Ref. [10] it was conjectured that the electron response to the THz electric field can be essentially modified near rare strong scattering centers or inhomogeneities [4,45–51] mediating a near-field coupling between the two helicity modes. Alternatively, near-field effects may originate from scattering of the plane EM wave itself, i.e., on charged or dipole centers in the dielectric matrix surrounding the 2DES. The development of quantitative theory models, determination of the near-field sources, and direct detection of emergent evanescent fields remain major objectives of future work which are outside the scope of this study.

On the other hand, an important result of this work is that the CRA/CRI ratio $\mathscr{R}^{AI}$ [Eq. (1)] is sensitive to the radiation power [see Figs. 2(d) and 5(c)]. It grows with lowering power and reaches values considerably larger than unity at low powers. Thus, the most puzzling *complete polarization immunity* is observed only at high powers, where it can be readily explained as a result of nonlinear electron heating, as outlined above. These observations are also in agreement with previous reports of complete polarization immunity in ultra-high-power measurements of the photoresistance response to pulsed THz radiation [9]. The revealed strong intensity dependence of $\mathscr{R}^{AI}$ should be helpful for identifying the mechanism of anomalous CRI absorption as, in the linear intensity regime, it is now sufficient to explain the emergence of resonant CRI signal that is several times weaker than the regular CRA signal.

As discussed in Sec. III A, the intensity dependence of the CRA/CRI ratio originates from different absorption strengths in the CRA and CRI regimes, which translate to different saturation powers P_s entering Eq. (2). For instance, analysis of the data shown in Fig. 2(d) gives a factor of 2 for the ratio P_s^{CRI}/P_s^{CRA} of saturation powers, consistent with the ratio of the linear coefficients a^{CRA}/a^{CRI}. Consequently, at high power the extrapolated ratio $\mathscr{R}^{AI}$ in Eq. (2) approaches unity. Comparing the photoresistance data obtained at two frequencies (see Figs. 2 and 5), we found that the saturation powers P_s are similar in both cases, while the corresponding saturation intensity is several times larger at higher frequency. Such increase is expected from the f^{-2} scaling of the Drude absorptance. Taken together, these observations suggest that, independent of the nature of the CRI absorption, the nonlinearity of the electron gas heating is observed when the absorbed radiation energy per unit area of the 2DES exceeds a certain value. This provides an additional evidence that the observed nonlinearities in the photoresistance are primarily associated with the nonlinearity of the energy losses $Q(I)$ which should be insensitive to the magnetic field as well as polarization and nature of the absorbed radiation.

Finally, we briefly comment on the observed anomalous helicity dependence of MIRO (see Figs. 6 and 7). In contrast to the resonant photoresistance caused by electron gas heating, MIRO amplitudes showed no saturation at elevated radiation

powers. Even at the lowest temperature ($T = 1.8$ K) they scale linearly both in CRA and CRI regimes [see Fig. 6(e)]. Correspondingly, the found CRA/CRI ratios $\mathscr{R}_M^{AI}$ for MIRO, varying in the range from approximately two to six depending on the sample and the experimental condition, were also almost independent of P [see Figs. 6(d) and 7(c)]. These findings are not surprising and are in line with the results of previous studies of this effect since the mechanisms of MIRO are not related to electron gas heating. These oscillations result from resonant absorption between neighboring or distant Landau levels broadened by disorder, which leads to an oscillatory correction to the energy distribution of electrons (inelastic mechanism) and spatial displacements of electron orbits in the direction determined by the ratio of radiation and cyclotron frequencies (displacement mechanism) [4]. At the same time, similar to the resonant photoresistance in the linear regime with respect to radiation power, MIRO are proportional to the radiation absorption. Therefore, the anomalous CRI absorption addressed above should affect the polarization dependence of MIRO in the same way as for the photoresistance induced by electron gas heating. Our studies indeed reveal similar CRA/CRI ratios for both the bolometric effect and MIRO, confirming that the anomalous helicity dependence of MIRO just reflects the anomalous resonant CRI absorption, and is not an inherent property of this effect [11].

V. SUMMARY

Summarizing, in our work we demonstrate that the recently observed helicity anomaly in resonant photoresistance, induced by the CR heating of the electron gas, possesses strong dependence on the power of the circularly polarized radiation. Namely, we observe that the CRA/CRI ratio in the photoresistance grows with lowering power, and show that this behavior is associated with the saturation of the resonant electron gas heating, characterized by different saturation powers for CRA and CRI magnetic field polarities. Importantly, even at lowest powers the CRA/CRI ratio remains anomalously low. The analysis of our results reveals that the overall behavior of the photoresistance is well captured by conventional theory including electrodynamic effects, such as strong metallic reflection from the 2DES in the region of the CR and the Fabry-Pérot interference in the substrate, combined with the standard theory of the electron gas heating. However, to get such an agreement, one needs to assume some source of resonant absorption in the CRI regime. While the observed anomalous behavior of the CR absorption and corresponding nonlinear photoresistance are of interest in their own right, the presented results are of importance for any polarization-sensitive photoelectric studies in 2DES.

[1] K. Seeger, *Semiconductor Physics: An Introduction* (Springer, Berlin, 2004).

[2] D. J. Hilton, T. Arikawa, and J. Kono, Cyclotron resonance, in *Characterization of Materials* (John Wiley & Sons, Ltd, 2012).

[3] M. A. Zudov, R. R. Du, J. A. Simmons, and J. L. Reno, Shubnikov–de Haas-like oscillations in millimeterwave photoconductivity in a high-mobility two-dimensional electron gas, Phys. Rev. B **64**, 201311(R) (2001).

[4] I. A. Dmitriev, A. D. Mirlin, D. G. Polyakov, and M. A. Zudov, Nonequilibrium phenomena in high Landau levels, Rev. Mod. Phys. **84**, 1709 (2012).

[5] D. A. Bandurin, E. Mönch, K. Kapralov, I. Y. Phinney, K. Lindner, S. Liu, J. H. Edgar, I. A. Dmitriev, P. Jarillo-Herrero, D. Svintsov, and S. D. Ganichev, Cyclotron resonance overtones and near-field magnetoabsorption via terahertz Bernstein modes in graphene, Nat. Phys. **18**, 462 (2022).

[6] I. A. Dmitriev, F. Evers, I. V. Gornyi, A. D. Mirlin, D. G. Polyakov, and P. Wölfle, Magnetotransport of electrons in quantum Hall systems, Phys. Status Solidi B **245**, 239 (2008).

[7] J. H. Smet, B. Gorshunov, C. Jiang, L. Pfeiffer, K. West, V. Umansky, M. Dressel, R. Meisels, F. Kuchar, and K. von Klitzing, Circular-polarization-dependent study of the microwave photoconductivity in a two-dimensional electron system, Phys. Rev. Lett. **95**, 116804 (2005).

[8] T. Herrmann, I. A. Dmitriev, D. A. Kozlov, M. Schneider, B. Jentzsch, Z. D. Kvon, P. Olbrich, V. V. Bel'kov, A. Bayer, D. Schuh, D. Bougeard, T. Kuczmik, M. Oltscher, D. Weiss, and S. D. Ganichev, Analog of microwave-induced resistance oscillations induced in GaAs heterostructures by terahertz radiation, Phys. Rev. B **94**, 081301(R) (2016).

[9] T. Herrmann, Z. D. Kvon, I. A. Dmitriev, D. A. Kozlov, B. Jentzsch, M. Schneider, L. Schell, V. V. Bel'kov, A. Bayer, D. Schuh, D. Bougeard, T. Kuczmik, M. Oltscher, D. Weiss, and S. D. Ganichev, Magnetoresistance oscillations induced by high-intensity terahertz radiation, Phys. Rev. B **96**, 115449 (2017).

[10] E. Mönch, P. Euringer, G.-M. Hüttner, I. A. Dmitriev, D. Schuh, M. Marocko, J. Eroms, D. Bougeard, D. Weiss, and S. D. Ganichev, Circular polarization immunity of the cyclotron resonance photoconductivity in two-dimensional electron systems, Phys. Rev. B **106**, L161409 (2022).

[11] M. L. Savchenko, A. Shuvaev, I. A. Dmitriev, S. D. Ganichev, Z. D. Kvon, and A. Pimenov, Demonstration of high sensitivity of microwave-induced resistance oscillations to circular polarization, Phys. Rev. B **106**, L161408 (2022).

[12] P. M. Mooney, Deep donor levels (*DX* centers) in III-v semiconductors, J. Appl. Phys. **67**, R1 (1990).

[13] M. Shur, *Physics of Semiconductor Devices* (Prentice-Hall, Englewood Cliffs, NJ, 1990).

[14] S. Sze, *Semiconductor Devices: Physics and Technology,* 2nd ed. (Wiley, India, 2008).

[15] G. W. Chantry, *Long-wave Optics: The Science and Technology of Infrared and Near-millimetre Waves* (Academic, London, 1984).

[16] S. D. Ganichev and W. Prettl, *Intense Terahertz Excitation of Semiconductors* (Oxford University Press, Oxford, 2005).

[17] E. Bründermann, H.-W. Hübers, and M. F. Kimmitt, *Terahertz Techniques* (Springer, Berlin, 2012).

[18] D. Kozlov, Z. D. Kvon, N. N. Mikhailov, S. A. Dvoretskii, and J. C. Portal, Cyclotron resonance in a two dimensional semimetal based on a Hgte Quantum well, JETP Lett. **93**, 170 (2011).

[19] M. Otteneder, I. A. Dmitriev, S. Candussio, M. L. Savchenko, D. A. Kozlov, V. V. Bel'kov, Z. D. Kvon, N. N. Mikhailov, S. A. Dvoretsky, and S. D. Ganichev, Sign-alternating photoconductivity and magnetoresistance oscillations induced by terahertz radiation in hgte quantum wells, Phys. Rev. B **98**, 245304 (2018).

[20] M. L. Savchenko, A. Shuvaev, I. A. Dmitriev, A. A. Bykov, A. K. Bakarov, Z. D. Kvon, and A. Pimenov, High harmonics of the cyclotron resonance in microwave transmission of a high-mobility two-dimensional electron system, Phys. Rev. Res. **3**, L012013 (2021).

[21] S. Hubmann, S. Gebert, G. V. Budkin, V. V. Bel'kov, E. L. Ivchenko, A. P. Dmitriev, S. Baumann, M. Otteneder, J. Ziegler, D. Disterheft, D. A. Kozlov, N. N. Mikhailov, S. A. Dvoretsky, Z. D. Kvon, D. Weiss, and S. D. Ganichev, High-frequency impact ionization and nonlinearity of photocurrent induced by intense terahertz radiation in HgTe-based quantum well structures, Phys. Rev. B **99**, 085312 (2019).

[22] S. Candussio, L. E. Golub, S. Bernreuter, T. Jötten, T. Rockinger, K. Watanabe, T. Taniguchi, J. Eroms, D. Weiss, and S. D. Ganichev, Nonlinear intensity dependence of edge photocurrents in graphene induced by terahertz radiation, Phys. Rev. B **104**, 155404 (2021).

[23] G. Abstreiter, J. P. Kotthaus, J. F. Koch, and G. Dorda, Cyclotron resonance of electrons in surface space-charge layers on silicon, Phys. Rev. B **14**, 2480 (1976).

[24] See Supplemental Material at http://link.aps.org/supplemental/10.1103/PhysRevResearch.6.023106 for similar experimental results obtained at several different conditions such as opposite radiation helicity or temperature.

[25] K. Chiu, T. Lee, and J. Quinn, Infrared magneto-transmittance of a two-dimensional electron gas, Surf. Sci. **58**, 182 (1976).

[26] S. A. Mikhailov, Microwave-induced magnetotransport phenomena in two-dimensional electron systems: Importance of electrodynamic effects, Phys. Rev. B **70**, 165311 (2004).

[27] Q. Zhang, T. Arikawa, E. Kato, J. L. Reno, W. Pan, J. D. Watson, M. J. Manfra, M. A. Zudov, M. Tokman, M. Erukhimova, A. Belyanin, and J. Kono, Superradiant decay of cyclotron resonance of two-dimensional electron gases, Phys. Rev. Lett. **113**, 047601 (2014).

[28] V. F. Gantmakher and Y. B. Levinson, *Carrier scattering in Metals and Semiconductors* (North Holland, Amsterdam, 2012).

[29] A. V. Muraviev, S. L. Rumyantsev, G. Liu, A. A. Balandin, W. Knap, and M. S. Shur, Plasmonic and bolometric terahertz detection by graphene field-effect transistor, Appl. Phys. Lett. **103**, 181114 (2013).

[30] M. Freitag, T. Low, F. Xia, and P. Avouris, Photoconductivity of biased graphene, Nat. Photonics **7**, 53 (2013).

[31] A. C. Betz, F. Vialla, D. Brunel, C. Voisin, M. Picher, A. Cavanna, A. Madouri, G. Fève, J.-M. Berroir, B. Plaçais, and E. Pallecchi, Hot electron cooling by acoustic phonons in graphene, Phys. Rev. Lett. **109**, 056805 (2012).

[32] J. N. Heyman, J. D. Stein, Z. S. Kaminski, A. R. Banman, A. M. Massari, and J. T. Robinson, Carrier heating and negative photoconductivity in graphene, J. Appl. Phys. **117**, 015101 (2015).

[33] V. Ryzhii, D. S. Ponomarev, M. Ryzhii, V. Mitin, M. S. Shur, and T. Otsuji, Negative and positive terahertz and infrared photoconductivity in uncooled graphene, Opt. Mater. Express **9**, 585 (2019).

[34] R. Jago, E. Malic, and F. Wendler, Microscopic origin of the bolometric effect in graphene, Phys. Rev. B **99**, 035419 (2019).

[35] D. Shoenberg, *Magnetic Oscillations in Metals* (Cambridge University Press, Cambridge, 1984).

[36] T. Ando, A. B. Fowler, and F. Stern, Electronic properties of two-dimensional systems, Rev. Mod. Phys. **54**, 437 (1982).

[37] M. Helm, E. Gornik, A. Black, G. Allan, C. Pidgeon, K. Mitchell, and G. Weimann, Hot electron Landau level lifetime in GaAs/GaAlAs heterostructures, Phys. B+C (Amsterdam) **134**, 323 (1985).

[38] G. A. Rodríguez, R. M. Hart, A. J. Sievers, F. Keilmann, Z. Schlesinger, S. L. Wright, and W. I. Wang, Intensity-dependent cyclotron resonance in a GaAs/GaAlAs two-dimensional electron gas, Appl. Phys. Lett. **49**, 458 (1986).

[39] Z. Mics, K.-J. Tielrooij, K. Parvez, S. A. Jensen, I. Ivanov, X. Feng, K. Müllen, M. Bonn, and D. Turchinovich, Thermodynamic picture of ultrafast charge transport in graphene, Nat. Commun. **6**, 7655 (2015).

[40] E. V. Beregulin, S. D. Ganichev, K. Y. Glukh, G. M. Gusev, Z. D. Kvon, A. Y. Shik, and I. D. Yaroshetskii, Submillimeter photoconductivity in inversion layers at a silicon surface, Pris'ma Zh. Eksp. Theor. Fiz. **48**, 247 (1988) [JETP Lett. **48**, 269 (1988)].

[41] E. V. Beregulin, S. D. Ganichev, K. Y. Glukh, G. M. Gusev, Z. D. Kvon, A. Y. Shik, and I. D. Yaroshetskii, Rapid submillimeter photoconductivity and energy relaxation of a two-dimensional electron gas near the surface of silicon, Zh. Eksp. Theor. Fiz. **70**, 2012 (1990) [Sov. Phys. JETP **70**, 1138 (1990)].

[42] A. Zayats, D. Richards, and D. Richards, *Nano-optics and Near-field Optical Microscopy*, Artech House Nanoscale Science and Engineering (Artech House, London, 2009).

[43] O. Keller, *Quantum Theory of Near-Field Electrodynamics*, Nano-Optics and Nanophotonics (Springer, Berlin, 2012).

[44] C. Girard and A. Dereux, Near-field optics theories, Rep. Prog. Phys. **59**, 657 (1996).

[45] E. M. Baskin, L. N. Magarill, and M. V. Entin, Two-dimensional electron-impurity system in a strong magnetic field, Zh. Eksp. Theor. Fiz. **75**, 723 (1978) [Sov. Phys. JETP **48**, 365 (1978)].

[46] A. V. Bobylev, F. A. Maaø, A. Hansen, and E. H. Hauge, Two-dimensional magnetotransport according to the classical lorentz model, Phys. Rev. Lett. **75**, 197 (1995).

[47] A. D. Mirlin, D. G. Polyakov, F. Evers, and P. Wölfle, Quasiclassical negative magnetoresistance of a 2D electron gas: Interplay of strong scatterers and smooth disorder, Phys. Rev. Lett. **87**, 126805 (2001).

[48] I. A. Dmitriev, A. D. Mirlin, and D. G. Polyakov, Oscillatory ac conductivity and photoconductivity of a two-dimensional electron gas: Quasiclassical transport beyond the Boltzmann equation, Phys. Rev. B **70**, 165305 (2004).

[49] Y. M. Beltukov and M. I. Dyakonov, Microwave-induced resistance oscillations as a classical memory effect, Phys. Rev. Lett. **116**, 176801 (2016).

[50] S. I. Dorozhkin, A. A. Kapustin, I. A. Dmitriev, V. Umansky, K. von Klitzing, and J. H. Smet, Evidence for non-Markovian electron dynamics in the microwave absorption of a two-dimensional electron system, Phys. Rev. B **96**, 155306 (2017).

[51] A. D. Chepelianskii and D. L. Shepelyansky, Floquet theory of microwave absorption by an impurity in the two-dimensional electron gas, Phys. Rev. B **97**, 125415 (2018).